

Graphical Abstract

On the wind-driven European shelf sea-level variability and the associated oceanic circulation

Sam T. Diabaté, Neil J. Fraser, Martin White, Barbara Berx, Louis Marié,
Gerard D. McCarthy

Highlights

On the wind-driven European shelf sea-level variability and the associated oceanic circulation

Sam T. Diabat , Neil J. Fraser, Martin White, Barbara Berx, Louis Mari , Gerard D. McCarthy

- Sub-annual sea-level variability is coherent throughout the shelf west of France, Ireland, and the United Kingdom.
- The along-isobath winds control this variability through convergence–divergence of the Ekman transport. The maximum sea-level changes are observed at the coastline.
- The spatial distribution of the sea-level changes yields variations in the geostrophic currents that we observe at the shelf-edge with a large dataset of independent in-situ measurements of the circulation.

On the wind-driven European shelf sea-level variability and the associated oceanic circulation

Sam T. Diabat  ^{a,b}, Neil J. Fraser^c, Martin White^d, Barbara Berx^e, Louis Mari  ^f, Gerard D. McCarthy^b

^a*Direction des Op  rations pour la Pr  vision, D  partement Pr  vision Marine et Océanographie (DirOP/MAR), M  t  o France, Toulouse, France*

^b*The Irish Climate Analysis and Research UnitS (ICARUS), Department of Geography, Maynooth University, Maynooth, Co. Kildare, Republic of Ireland*

^c*The Scottish Association for Marine Science (SAMS), Scottish Marine Institute, Oban, Argyll and Bute, Scotland, UK*

^d*University of Galway, Galway, Co. Galway, Republic of Ireland*

^e*Marine Directorate, Scottish Government, 375 Victoria Rd, Aberdeen, AB11 9DB, Scotland, UK*

^f*Univ. Brest, CNRS, IFREMER, IRD, Laboratoire d'Océanographie Physique et Spatiale (LOPS), IUEM, Plouzan  , F-29280, France*

Abstract

The shelf to the west of Ireland, France and the United Kingdom is a region where currents and sea level respond to the wind activity in a remarkable manner throughout a range of timescales. Using altimetry-obtained measurements and a wind reanalysis, we demonstrate in the present contribution how the sub-annual sea-level variability can be understood as a response to the wind action. The winds drive water towards (away from) the coastline through Ekman transport, yielding sea-level changes coherent along and across the shelf and with maximum amplitude at the coast. The alignment of the winds with the isobaths determines the magnitude of sea-level changes. To investigate the impacts of these changes on the circulation variability, we bring together a comprehensive dataset of 30+ in-situ observations of recent current changes. Using these measurements, we show that

sub-annual changes in the shelf-edge circulation from the Goban Spur to the Faroe–Shetland Channel arise from the geostrophic adjustment to shelf sea-level variations induced by the Ekman-driven accumulation of water towards the coastline. Our analysis suggests that the along-isobath current generated through this mechanism are primarily found over the shelf, only *impinge* on the upper slope, and do not affect the circulation above greater depth ($>500\text{m}$). Nonetheless, important slope circulations such as the Rockall Slope Current are substantially influenced on their shoreward side by this simple geostrophic adjustment process. Because sea-level changes co-vary over large distances on the shelf, there also is remarkable along-isobath coherence in the associated current changes but we warn against concluding this is evidence for the continuity of an ‘European Slope Current’ circum-navigating the European slope from Portugal to Norway.

Keywords: Sea-level changes, Shelf variability, In-situ currents, Wind forcing, Rockall Slope Current, European Slope Current, Sub-annual timescales.

¹ 1. Introduction

² Above and around the continental shelf to the west of France, Ireland,
³ and the United Kingdom (UK), the forcing action of atmospheric variability
⁴ is well known to affect oceanic currents and sea level (Chafik et al., 2017;
⁵ Pingree et al., 1999; Gordon and Huthnance, 1987; Le Boyer et al., 2013;
⁶ Plag and Tsimpis, 1999; Chafik et al., 2019; Calafat et al., 2012). In par-
⁷ ticular, wind stress exerts an important control on shelf and slope dynamics
⁸ throughout a range of timescales, from those associated to localised storms

⁹ (Gordon and Huthnance, 1987) to those associated with large-scale atmospheric modes (*e.g.* the North Atlantic Oscillation, see Chafik et al., 2019).
¹⁰ Large uncertainties remain over the nature of shelf-wide coherent sea-level
¹¹ changes at sub-annual timescales, how they respond to along-isobath wind
¹² stress, and the consequences for shelf and slope circulation.
¹³

¹⁴ Chafik et al. (2017) showed the monthly sea level variability on the North-west European Shelf included a shelf-scale common mode extending from
¹⁵ Portugal to Norway driven by atmospheric variability. Typical sea-level variations associated with the mode were of a few centimetres west of France,
¹⁶ Ireland and the United Kingdom. Greater variations were observed in the
¹⁷ North Sea. Chafik et al. (2017) demonstrated that this mode was related
¹⁸ to the alignment of winds with the continental slope to the west and north
¹⁹ of Europe. They however found regional differences, associated to different
²⁰ fingerprints of the atmospheric variability modes. Similarly, Hogarth et al.
²¹ (2020) extracted the common variability in British-Irish Isles monthly tidal
²² record residuals and presented a map of correlation with sea surface height.
²³ The common mode extended in a cross-slope sense from the shelf edge to the
²⁴ coast; and in an along-slope sense from south and east of the Canary Islands
²⁵ thousands of kilometres upstream, to the Faroe-Shetland Channel. Hogarth
²⁶ et al. (2020) hypothesised changes in along-slope winds were the likely driver.
²⁷ The Hogarth et al. (2020) and Chafik et al. (2017) modes projected differ-
²⁸ ently in the southern North Sea and in the Greenland-Iceland-Norwegian
²⁹ basin. Nonetheless, west of France, Ireland and the UK, the two were con-
³⁰ sistent.
³¹
³²

33 Chafik et al. (2017) proposed that the wind-driven on-shelf sea-level vari-
34 ations were reflected in changes in the eastern boundary slope current cir-
35 cumnavigating the European shelf through geostrophic adjustment. The
36 mechanism linking the wind-driven shelf sea-level variability and boundary
37 circulation is relatively simple — at least for largely subinertial flow. It is
38 that of winds accumulating (removing) water onto (from) the shelf through
39 Ekman transport, rising (lowering) shelf sea elevation and creating an across-
40 slope pressure gradient. Geostrophic equilibrium suggests a boundary current
41 balances this gradient. The cross-slope position of such a current depends on
42 the exact response of the slope and shelf sea level to the wind forcing, with
43 bottom friction playing a role (Huthnance, 1986a).

44 While it is clear that Ekman currents lead to accumulation (removal) of
45 water onto (from) the shelf and affect the on-shelf sea level, the study of
46 the associated acceleration or deceleration of longshore geostrophic flow is
47 often omitted. In recent decades, a number of observational programs have
48 measured the circulation variability around the European margin, providing
49 means to fill this knowledge gap. In the present contribution, we characterise
50 the shelf-wide coherent sea-level changes at sub-annual timescale, identify
51 how they are a response to the stress imposed by along-isobath winds, and
52 investigate the consequences for the shelf and slope circulation. We focus
53 on timescales shorter than a year but large with respects to the inertial
54 frequency. Section 2 presents the data used and editing performed. An
55 analysis of sub-annual sea surface height variability, its link with the wind
56 changes, and its effects on currents is presented in Section 3. We discuss our
57 results in Section 4 and we conclude in Section 5.

58 **2. Data and method**

59 *2.1. Generalities*

60 The Northwest European Shelf is a wide shelf. The general bathymetry
61 of this region is presented in Figure 1. Throughout this paper, we use the
62 following limits to define bathymetry regions west of France, Ireland and
63 the United Kingdom. The abyssal plain and the continental rise are de-
64 fined as regions where water depth exceeds 2000m. The lower, intermediate
65 and upper slope range from 2000m to 1000m, from 1000m to 500m, and
66 from 500m to 200m respectively. The shelf-edge at 200m separates the up-
67 per slope and the shelf. We further separate the shelf into the outer-shelf
68 (depth>100m) and the inner-shelf (100m>depth>0m). The definition of the
69 shelf-edge at 200m is rather classic (*e.g.*, Xu et al., 2015) and this depth ap-
70 proximately corresponds to where the cross-shelf slope changes dramatically.
71 Finally, upstream and downstream are meant with respect to the propaga-
72 tion of coastally trapped waves. In this eastern boundary context, upstream
73 is always equatorward and downstream, poleward.

74 *2.2. Sea level and surface geostrophic currents*

75 The sea surface height above geoid was retrieved from the Copernicus Ma-
76 rine Environment Monitoring Service (CMEMS) SEALEVEL_EUR_PHY_L4_MY_008_068
77 regional product, available at <https://doi.org/10.48670/moi-00141>. This
78 product was previously used in a recent study of the Rockall Slope Current
79 and Rockall Trough transport (Fraser et al., 2022). It has a horizontal spacing
80 of $1/8^\circ \times 1/8^\circ$ obtained through optimal interpolation merging of processed
81 along satellite track altimeter measurements and covers the period 1st Jan-

82 January 1993–31st December 2021. These processed along-track inputs have
83 numerous corrections already applied. These include de-tiding, dynamical
84 atmospheric correction (DAC), and more (Pujol et al., 2023). For the fre-
85 quency band considered in the present work, the DAC consists solely of an
86 adjustment for the inverse-barometer effect.

87 Although distributed with daily timesteps and on a $1/8^\circ \times 1/8^\circ$ grid,
88 the altimetry data has coarse effective spatial and temporal resolution due
89 to the mapping methodology and the satellite constellation configuration.
90 Ballarotta et al. (2019) found effective temporal resolution to lie between 14
91 and 28 days around northwest Europe for a global daily SSH product with
92 $1/4^\circ \times 1/4^\circ$ spatial grid (see their Figure 3). To the best of our knowledge,
93 there is no estimate of effective temporal resolution for the European regional
94 product, but it can be anticipated to be equivalent or marginally better. For
95 this reason, we restrict our attention to cycles longer than 20 days. Pujol
96 et al. (2023) report, for the $1/8^\circ \times 1/8^\circ$ product we use, effective spatial
97 resolutions of 200 kilometres or less west of France, Ireland and the UK (see
98 their Figure 15). This means oceanic features of 50km radius/spatial scale
99 are accurately represented ($0.25 \times$ effective resolution, see Ballarotta et al.,
100 2019), provided they lasted for long enough. In comparison, the shelf has
101 a cross-slope width ranging from \sim 50km off Erris Head (Ireland, $10^\circ 0.2W$,
102 $54^\circ 18.4N$) to \sim 400km off the tip of Cornwall (UK).

103 Sea surface height derived from satellite altimetry can be problematic at
104 immediate proximity of the coastline. To validate our results, we retrieved
105 tide gauge monthly timeseries from the Permanent Service for Mean Sea
106 Level (Permanent Service for Mean Sea Level, 2023; Holgate et al., 2013,

dataset downloaded on 13th February 2023). We only make use of Revised Local Reference (RLR) data, and select tide gauges with no more than 20% missing values over a lifespan of at least 10 years within the 1993–2022 period. Additionally, we obtained from the Irish National Tide Gauge Network (INTGN) tidal records from three tide gauge sites located along the coast of the Republic of Ireland. These records are unavailable on the PSMSL website but match the above criteria of completeness and duration. They are Howth, at proximity of Dublin in the Irish Sea; Castletownbere southwest of Cork; and Galway, facing the open Atlantic ocean. A static inverse barometer contribution is removed from all tide gauge records.

2.3. Atmospheric sea-level pressure and winds

Daily mean horizontal wind speeds at 10m above the mean sea surface were obtained from the The NCEP/DOE AMIP-II Reanalysis (Kanamitsu et al., 2002, NOAA PSL, Boulder, Colorado, USA, <https://psl.noaa.gov>, last access: 08 August 2022) for the period January 1993–December 2021 and converted to wind stresses.

Monthly mean surface pressure, also obtained from the NCEP/DOE AMIP-II Reanalysis (Kanamitsu et al., 2002), were used to correct the tide gauge records for the inverse barometer effect, assuming an isostatic response.

2.4. In-situ currents from moored deployments

Our analysis relies on data from Single-Point Current-Meters (SPCMs) and Acoustic Doppler Current Profilers (ADCPs) moored on the shelf and slope west of France, the Republic of Ireland, and the United Kingdom. We restrict our attention to deployments carried out since the start of the

131 altimetry era in 1993, for comparison with sea surface height. ADCP and
132 SPCM data were obtained from numerous historic and ongoing observational
133 programs, including new data from the recent Irish Ocean Observing System
134 (EirOOS). Details on mooring data are given in Appendix A.

135 Modern ADCPs and SPCMs internally perform a non-negligible level of
136 initial editing including coordinate transform, quality control and ensemble
137 averaging. The data obtained after this initial editing is an ideal and suffi-
138 ciently upstream source. We then perform the following processing workflow,
139 which is a twice-repeated combination of interpolation and low-pass filtering.
140 At each mooring site, data from sensors installed at different depths or from
141 different deployments at the same site are merged. A depth-time interpola-
142 tion based on a Delaunay triangulation allows to re-grid horizontal velocities
143 on a regular mesh and eliminate blow-down effects. The query grid has 10-
144 metre depth-increments and hourly timesteps. Interpolation is performed
145 only for depth-time query coordinates falling within triangles of inter-vertex
146 distances inferior to three hours and half the water column depth or 300m
147 (whichever is the largest). Query points not meeting these thresholds are
148 omitted. The obtained horizontal velocities are convoluted with a 3-day
149 Tukey window and daily averaged. This low-pass filters the velocities and
150 effectively removes the tidal signal. Once de-tided, the data has considerably
151 greater temporal auto-correlation. It is again interpolated using a Delaunay
152 triangulation, but this time allowing for greater inter-vertex distances in time
153 (up to ten days). Finally, the obtained velocities are convoluted with 20-day
154 Tukey window to focus on low-frequency variability and for consistency with
155 the sea surface height data. The regularly gridded and low-pass filtered cur-

156 rents are depth averaged from the surface to the 500 metre level (or the
157 bottom if shallower). The rationale for such averaging is that currents in the
158 northeast Atlantic margin are very vertically coherent in this depth range.
159 Note the gaps in the in-situ current data as well as the various deployment
160 durations do not allow to remove seasonality or lower frequency variability.
161 For each timesteps, if missing data represents a significant fraction of the
162 water column (more than 50%), the whole average is considered as missing.

163 The above-described processing stream was performed for all mooring
164 lines equipped with several SPCMs and/or at least one ADCP. RT-EB0,
165 NWZF and NWZH are three mooring sites equipped with bottom mounted
166 upward-looking ADCP which do not meet our completeness threshold for
167 extended amounts of time. For these moorings, we swap the depth-average
168 estimates for currents at a given depth level instead (respectively, 500m,
169 180m and 160m). Lastly, we augment our dataset with three mooring sites
170 with data available from only one SPCM, but which fill in geographical gaps.
171 They are OMEX moorings WBNE, WBSW and PML-150 (see Appendix
172 A). For these moorings, velocities are simply binned at a nominal depth and
173 convoluted with a 20-day Tukey window. Table 1 presents a summary of
174 all 36 mooring data used, and Figure 2 presents temporal coverage for each
175 mooring individually.

176 In Figure 1 current standard deviations, obtained through principal com-
177 ponent decomposition (see Appendix C), are represented as ellipses. The
178 semi-major and semi-minor ellipse radii indicate the amplitude of the stan-
179 dard deviation of current deviations from the mean flow. The semi-major axis
180 orientation indicate the principal direction of variance. The currents show

181 considerable variance at all sites, also with a poleward increase in magnitude.
182 The main direction of variance is everywhere aligned with local isobaths. We
183 observe a greater topographical steering at slope and coastal mooring sites
184 than at outer-shelf and abyssal locations. The peculiar bathymetry of the
185 Goban Spur leads to a singular zone where little topographical steering can
186 be observed, with the variance ellipse making up an almost perfect circle at
187 EBS1 (approx. 12°E, 49°N). The same observations can be drawn from the
188 record obtained from PML-154 mooring, which was also located above the
189 1000m isobath on the Goban Spur (the two mooring positions coincide, but
190 there are 20+ years between deployments).

191 *2.5. In-situ currents from underwater gliders*

192 In recent years, the Overturning in the Subpolar North Atlantic Program
193 (OSNAP) has integrated underwater glider observations, which are used to
194 accurately estimate hydrography and transport at the eastern boundary of
195 the array (Fraser et al., 2022). The gliders cross the slope from the RT-EB1
196 mooring position above a depth of \sim 1800 metres, to the shelf edge and allow
197 for an unprecedented spatial resolution. Fraser et al. (2022) derived along-
198 slope velocity estimates from the thermal wind shear referenced to the mean
199 horizontal velocity derived from the glider deflection off course between con-
200 secutive GPS fixes. The nominal resolution of their product is $dx = 250\text{m}$.
201 The effective horizontal resolution is determined by the distance between re-
202 peated glider dives/ascent and is on the order of 3km. It gets better with
203 shallowing bathymetry, as can be seen on Figure 2b of Fraser et al. (2022).
204 The temporal resolution is on the order of two transects per week. We inter-
205 polate Fraser et al. (2022) estimate on regular time intervals by employing

206 an inverse distance-weighting technique, where the power parameter is set
207 to $p = 2$ and a 20-day search radius is used. The velocities are then depth-
208 averaged, and, to focus on the low-frequency variability, convoluted with a
209 20-day Tukey window.

210 **3. Analysis**

211 *3.1. Shelf sea-level variability and associated geostrophic flow*

The altimetry-derived sea-level anomaly η is objectively decomposed into variability modes of decreasing importance using empirical orthogonal function analysis,

$$\eta(x, y, t) = \sum_{i=1}^n \phi_i(x, y) \alpha_i(t), \quad (1)$$

212 after a 20–360 day bandpass filter is applied at each gridpoint. The North Sea
213 is not considered, to focus on the variability to the west of the UK, Ireland
214 and France. The bandpass filtering method removes the mean seasonal cycle
215 in the sea surface height data, but does not correct for any seasonal cycle in
216 the variance or higher-moment statistics. This minor problem is discussed in
217 Appendix E. The time-varying principal components (PCs) α and spatially
218 varying empirical orthogonal vectors or functions (EOFs) ϕ together make
219 up the modes $i = 1, 2, 3, \dots, n$. To focus on coherent signal of large spatial
220 scale in sea surface height field, we discuss the leading mode $i = 1$, associated
221 with the pair $\phi_1 \cdot \alpha_1$. Note that principal component analysis is well-known
222 to be dependent on the domain extent and on spatial differences in variance
223 and skewness (Monahan et al., 2009). Here, we decided to exclude the North
224 Sea from our analysis because its variability is different from the region west
225 of France, Ireland and the UK. For example, the two regions are affected

226 differently by atmospheric mode teleconnections (Chafik et al., 2017). These
227 differences are not easily captured using (covariance-based) EOF decompo-
228 sition because the sea-level variance in the North Sea is much greater than
229 (say) west of France.

230 Figure 3a. shows the leading EOF ϕ_1 , which is positive over the entire
231 shelf. This represents the in-phase, coherent sea-level variations. The gen-
232 eral picture is that of maximum amplitudes at the coast and gently decaying
233 oceanward, up to the slope where they vanish ($\phi_1 \sim 0$). Broadly speaking,
234 ϕ_1 follows bathymetry contours, with some bathymetric features distin-
235 guish-
236 able (Goban Spur, Porcupine Seabight, Porcupine Bank, the gentle slope of
237 the outer Celtic shelf, etc.). In addition, ϕ_1 increases poleward along the
238 coast, with maximum values found in the northern Irish Sea and on the in-
239 ner Scottish shelf. In total, the mode accounts for 16% of the sea surface
240 height variance over the domain, but the fraction of variability explained is
241 much greater over the shelf, particularly around Ireland and west of the UK
242 (Figure 3b., we return to this point further below). On the other hand, the
243 open ocean variability is largely unexplained by the mode (Figure 3b.) —
244 and reversely, the open ocean makes little contribution (Figure 3a.). This is
245 expected, because at the timescales considered here, the open ocean sea sur-
246 face height variability largely reflects eddying activity which is not coherent
over large spatial regions.

The horizontal gradients of ϕ_1 are associated with surface geostrophic
anomalous currents which can be readily derived using

$$\mathbf{v} = -g\mathbf{k} \times \nabla(\phi_1)/f, \quad (2)$$

247 where \mathbf{k} is the unitary vertical vector. The velocities are generally orien-

tated along-isobath and increase poleward in magnitude (Figure 3c). The anomalous currents flow poleward when the sea-level anomaly is positive over the shelf. Northwest of Ireland as well as west and north of Scotland, broad, strong current jets can be observed. There, strong velocities encompass the whole shelf. They also encompass a significant part of the slope. However, this feature is likely introduced by the optimal interpolation involved in the generation of the gridded sea surface height product which tends to smooth sharp sea surface height gradients, typically found above sharp bathymetry gradients. From 54°N to 51°N, strong current anomalies are limited to the east of the saddle point and Porcupine Seabight — they do not extend around the Porcupine Bank. From 51°N to the southern Bay of Biscay, current anomalies are diffuse and relatively weaker than to the north. In this region there exists two distinct circulation patterns associated with the mode: a coastal pathway perceptible along the Brittany coast, west of the tip of Cornwall and flowing towards Ireland, and a well separated slope pathway.

The associated principal component α_1 is shown in Figure 4a. It explains between 40 and 80% of the sea surface height variability over the shelf north of 47° N (Figure 3b.), which indicates its usefulness to help the analysis of shelf sea-level variability and, we argue, current changes. It features important fluctuations, putting in perspective the values taken by ϕ_1 and \mathbf{v} which are relative to periods when $\alpha_1 = 1$. The peak-to-peak amplitude (maximum value minus minimum value) of α_1 is ~ 8.4 , associated to $\pm 14\text{--}20\text{cm}$ sea-level change in the northern Irish Sea and along the western Scottish coast and up to $\pm 15\text{cm.s}^{-1}$ surface geostrophic current change northwest of the

273 Outer Hebrides. However, this range reflects extremum positive and negative
274 figures which occurred only once over the observation period. In Figure
275 4b. and c. we present the distribution of values taken by α_1 , together
276 with its probability of being below a given threshold (which is simply the
277 accumulated distribution). One week per year on average, the principal
278 component is found above a value of +2, associated with sea elevation $\geq 9\text{cm}$
279 above the background state in the northern Irish Sea and Scottish inner-shelf
280 and anomalous surface geostrophic current $\geq 7\text{cm.s}^{-1}$ northwest of the Outer
281 Hebrides. A week every ten years, the principal component is above +3,
282 that is an anomalous sea elevation $\geq 10\text{cm}$ and anomalous surface geostrophic
283 currents $\geq 11\text{cm.s}^{-1}$ in the same regions.

284 To show that the shelf common mode extends all the way to the coast-
285 line, the tide gauge timeseries were regressed against the monthly-averaged
286 principal component α_1 . Prior to this operation, the tide gauge records were
287 linearly detrended, their seasonal climatological cycle was subtracted and
288 a 11-month running mean (tolerant to missing values) was removed. The
289 obtained regression coefficients, shown as circular markers in Figure 3a. rep-
290 resents how much sea-level variability within this mode projects to the coast.
291 The markers are almost identical to their nearestmost ϕ_1 value, indicating
292 the relevance of the common mode even at the coastline.

293 *3.2. Source of the shelf variability*

294 Numerous studies have highlighted the role of winds in driving Northwest
295 European Shelf variability throughout a range of timescales (Gordon and
296 Huthnance, 1987; Chafik et al., 2017; Pingree and Le Cann, 1989; Pingree
297 et al., 1999; Le Boyer et al., 2013; Plag and Tsimpis, 1999; Hermans et al.,

298 2020; Calafat et al., 2012; Chafik et al., 2019). Therefore, we compare in this
299 section the coherent sea surface height variability associated with $\phi_1 \cdot \alpha_1$ with
300 changes in the atmospheric circulation.

The physical response of the ocean to the wind stress action yields the observed sea-level variability $\alpha_1(t)$. We model this process as a linear and time-independent response (we effectively assume $\alpha_1(t)$ is fully wind driven),

$$\alpha_1(t) = \frac{1}{S} \iint_S \mathbf{K}(x, y) \cdot \boldsymbol{\tau}(x, y, t) dx dy, \quad (3)$$

301 where $\mathbf{K} = (K^x, K^y)$ is a vector field representing the sensitivity of α_1 to
302 the surface wind stress anomaly $\boldsymbol{\tau} = (\tau^x, \tau^y)$ at any given point (x, y) . This
303 sensitivity is sought using a Principal Component based Multiple Linear
304 Regression approach (PCMLR, see Appendix D below and Mendes, 2009).

305 Figure 5a. presents \mathbf{K} , the sensitivity of the ocean to the forcing action
306 of the wind stress changes. Over the shelf and slope to the south of Ireland
307 and west of France, large \mathbf{K} vectors aligned with isobaths are seen. They
308 are significant above 99% threshold (details on how significance is obtained
309 are given in Appendix D). On Figure 5 b. to d., we present the wind-
310 based reconstruction of the shelf sea-level variability obtained with Equation
311 D.1 after masking out non-significant grid-points and grid-points outside of
312 the 18° W, 44° N to 00° W, 60° N box. This reconstruction compares very
313 favourably with α_1 (correlation is $r = 0.66$). Altogether, these results high-
314 lights that along-isobath winds in the shelf and slope regions to the west of
315 France and south of Ireland are the primary driver of changes in α_1 .

316 *3.3. Response of currents to sea surface height changes*

317 Figure 6 highlights great agreement from the Goban Spur to the Faroe-
318 Shetland Channel between α_1 and current variability over the upper-slope
319 and outer-shelf. In the Faroe-Shetland Channel (Panel a.), high correlations
320 are seen at NWSF, NWSH, NWZH, and NWZF ($r = 0.43, 0.58, 0.59$ and 0.55
321 respectively, all significant). A visual inspection of the velocity timeseries
322 together with that of the common mode principal component α_1 highlight
323 differences but general agreement (Figure 7a. and b.). On the Hebridean
324 slope (Figure 6 b.), correlations and significance between α_1 and the depth-
325 averaged along-isobath velocities obtained from the repeated glider transects
326 at 57°N (Fraser et al., 2022) increase almost monotonically with decreasing
327 depth up to a maximum value at the shelf edge (~ 200 metres). Significant
328 correlations (above 95%) are found within one kilometre of the shelf-edge,
329 approximately corresponding to correlation superior to 0.35. In effect, the
330 glider-obtained velocities averaged in the 365–195m isobath range show pe-
331 riods of strong agreement with the common mode (*e.g.*, June–July 2020,
332 October 2020–January 2021, November 2021) and a period of no agreement
333 at all (April–May 2021, see Figure 7c.). The elevated and outlying spring
334 2021 velocity values can be related to the presence of two consecutive and
335 long-lived eddies in the zone, also observed at RT-EB1 (See Figure 16.10 of
336 Moat et al., 2022). Farther south, at $56^\circ28\text{N}$, depth-averaged flow at S140
337 and S400 agree well with the common mode, with correlation of $r = 0.47$ and
338 $r = 0.78$ respectively, significant at 98% and >99% (Figure 6b. and Figure
339 7d.). Southwest of Ireland, a strong correlation is seen between α_1 and the
340 along-isobath currents measured by the upper SPCM (30 metres below sur-

341 face) at PML-150 $r = 0.65$, significance is 93%, only slightly below the 95%
342 threshold, see Figure 6c. and Figure 7d.).

343 During the September 1995–October 1995 period, increase in along-isobath
344 anomalous flow at PML-150 on the Goban Spur outer-shelf was concurrently
345 observed at S400 and S140 on the Hebridean upper slope and outer shelf
346 (Figure 7 d.). During this period, α_1 went from a negative to a positive
347 phase which was associated with sea-level rise on the shelf and translated
348 in increased anomalous surface geostrophic currents. This further demon-
349 strates that shelf sea-level variations are responsible for along-isobath coher-
350 ence along the shelf-edge.

351 In the intermediate slope depth range (1000–500m), correlations are lower
352 (NWE line, NWSD, RT-EB0, S700, WBNE, WBSW) and in general non-
353 significant. This reflects the lessening of the shelf sea-level influence on cur-
354 rents; or alternatively the increasing dominance of other sources of variability
355 at this depth range. In even deeper water, current variability does not reflect
356 the shelf mode at all (RT-EB1, SRT, PML-154, EBS1, GS-EB1). Finally,
357 farther south in the Bay of Biscay, no significant agreement is found between
358 in-situ current observations and the common mode of sea-level variations
359 regardless of the depth range.

360 The general picture at the outer-shelf and upper-slope is that of an agree-
361 ment between on-shelf sea-level variability and along-isobath in-situ currents
362 from the Faroe-Shetland Channel to the Goban Spur (Figure 6). The agree-
363 ment decreases sharply with depth across the slope.

364 **4. Discussion**

365 We identified coherent sub-annual sea surface height changes on the shelf
366 from the Bay of Biscay to the Faroe-Shetland Channel, well separated from
367 the open ocean variability. The spatial fingerprint of the common sea-level
368 variability is that of elevated amplitudes at the coastline, decaying gently
369 across the shelf and sharply decreasing to zero magnitude offshore of the
370 shelf-edge towards the abyssal ocean. These coherent sub-annual sea-level
371 fluctuations are in excess of 9cm above background mean sea level one week
372 per year on average in the Irish Sea and along the Scottish coastline. Winds
373 were shown to drive these shelf-wide variations, which contribute to extreme
374 sea levels along the seabards of France, the UK and Ireland. Specifically,
375 the alignment of winds with local isobaths in the region west of France and
376 south of Ireland was found to play a key role.

377 Our analysis shares some similarity with past works that focused on
378 the monthly sea-level variability over the Northwest European Shelf (Chafik
379 et al., 2017; Hogarth et al., 2020). Chafik et al. (2017) suggested the coherent
380 shelf sea-level variability drove changes in the boundary circulation, but this
381 was never checked with in-situ data as was done here. We generally found
382 that, as hypothesised by Chafik et al. (2017), depth-averaged currents over
383 the outer-shelf and upper-slope balance the coherent shelf sea-level changes
384 from the Goban Spur to the Faroe-Shetland Channel. The along-isobath
385 velocities at SES sites and Faroe-Shetland Channel moorings were known to
386 be in agreement with local surface geostrophic flow (Xu et al., 2015; Berx
387 et al., 2013), but we highlight the specific role of the common shelf sea-level
388 variability in driving the outer-shelf and upper-slope geostrophic circulation,

389 which is not simply local and extends thousands of kilometres along isobath.
390 This was not previously shown.

391 The general physical mechanism is that shelf sea-level variations, estab-
392 lished from the mass convergence and divergence associated to the wind-
393 driven Ekman transport, must be balanced by the Coriolis force. This means
394 that elevated sea levels on the shelf lead to accelerated geostrophic along-
395 isobath currents. In practice, the winds set up coastally trapped waves, but,
396 at long enough timescales, development is nil ($\partial_t \sim 0$), and these waves are
397 arrested. Simply put, this means the characteristic wave speeds are consider-
398 ably faster than the wind changes, so that an equilibrium is reached virtually
399 instantaneously, and the timescale of changes in sea level and currents is im-
400 posed by the wind forcing. The spatial structure of ϕ_1 — roughly a function
401 of the seabed depth alone, with amplitudes maximum at the coast, decaying
402 gently oceanward and abruptly vanishing at the slope — reminds of the char-
403 acteristic fingerprints of continental shelf waves. Continental shelf waves are
404 shelf topographic Rossby waves (Gill and Clarke, 1974; Mysak, 1980; Huth-
405 nance, 1986a; Gordon and Huthnance, 1987; Hughes et al., 2019) known to
406 ‘couple well with the wind forcing’ (Huthnance, 1986a). In their mode-1,
407 they include the coastal Kelvin wave and have sea-level amplitude maximal
408 at the coast (for low frequency – large wavelength, see Huthnance, 1986a,b;
409 Gordon and Huthnance, 1987), quite similarly to the pattern shown in Figure
410 3a. Note we found the region where sea-level changes associated with the
411 mode are the largest (in the Irish Sea and along the Scottish coastline) is
412 poleward of the region where the wind alignment with the local isobaths is
413 most determinant to changes in α_1 (west of France and south of Ireland). The

414 latter is an area where large along-coast growth in ϕ_1 is observed. Both these
415 findings are extremely consistent with the cyclonic propagation of coastally
416 trapped waves and the cumulative effect of the longshore wind forcing along
417 isobath (Calafat et al., 2012; Gill and Clarke, 1974).

418 **5. Conclusion**

419 Wind-driven sea-level variability on the shelf can be related to circula-
420 tion changes at the outer-shelf and upper-slope at subannual scales — and
421 likely beyond, at faster and slower periodicities (Hermans et al., 2020; Chafik
422 et al., 2019; Calafat et al., 2012; Gordon and Huthnance, 1987). The shelf
423 sea-level variability is one of the key contributors to along-slope coherence in
424 currents over thousands of kilometres along the European margins. Broadly
425 speaking, a bathymetry-following, poleward (equatorward), anomalous flow
426 can be expected to occur when elevated (depressed) sea levels relative to
427 normal are found over the shelf. These shelf sea-level changes arise due to
428 the convergence of Ekman currents in the presence of a sloping bathymetry
429 and/or a coastline. Our results indicate that sea-level changes driven by Ek-
430 man transport and converted into along-isobath current through geostrophic
431 adjustment are of prime importance for the European margin circulation.

432 While shelf sea-level variability generates anomalous geostrophic circula-
433 tion, our results indicate these currents are limited to the upper slope and
434 shelf. Coherent shelf sea-level changes are hence associated with a boundary
435 circulation flowing east of the Porcupine Seabight and through the Porcu-
436 pine Saddle Point rather than around the Goban Spur and the Porcupine
437 Bank. This shallow pathway has sometimes been associated with the con-

tinuous ‘European Slope Current’ (Xu et al., 2015; Pingree et al., 1999), yet we recommend caution when using this term. Thus far, representations of a continuous circulation trapped at the shelf-edge and extending from Portugal (if not more to the south) to the Faroe-Shetland Channel (or more to the north) were derived from sea surface height anomalies rather than mean values (our Fig. 3b., as well as Fig. 6a. of Xu et al. 2015 or Figure 16 of Pingree et al. 1999). The mean sea surface height distribution in the region is rather different, and cannot be associated with poleward surface geostrophic flow over the slope to the south of Ireland (Diabat   et al., in prep.). Generally speaking, the continuity of a slope circulation along European margins remains debated. Nonetheless, the poleward current locked to the eastern continental slope of the Rockall Trough (the Rockall Slope Current after Huthnance, 1986a, although it bears many other names), is influenced on its shoreward side by the anomalous flow associated with the common shelf sea-level variability.

6. Acknowledgements

S. T. Diabat   and G.D. McCarthy work within the A4 project (Grant-Aid Agreement No. PBA/CC/18/01) which is carried out with the support of the Marine Institute under the Marine Research Programme funded by the Irish Government. This study is a contribution to the Climate Linked Atlantic Section Science (CLASS) programme and was in part supported by the UK Natural Environment Research Council National Capability funding (NE/R015953/1).

EirOOS (the Irish Ocean Observing System) is supported in part by Sci-

462 ence Foundation Ireland under Grant No. 18/RI/5731. Data from the LOIS-
463 SES and OMEX programs were provided by the British Oceanographic Data
464 Centre (BODC) and funding sources are indicated in Souza et al. (2001);
465 Huthnance et al. (2001); White and Bowyer (1997) or references therein. Fur-
466 thermore, our work makes use of data collected with the support of the Flotte
467 Océanographique Française, during the ASPEX series of cruises (<https://doi.org/10.18142/245>). Moored instruments in the Faroe-Shetland Chan-
468 nel have been supported by the Offshore Monitoring Programme of Scottish
469 Government's Marine Directorate and by European Framework Programmes
470 under grant agreement No. GA212643 (THOR) and grant agreement No.
471 308299 (NACLIM), and from the European Union's Horizon 2020 research
472 and innovation programme under grant agreement No. 727852 (Blue-Action),
473 as well as the Nordic WOCE, VEINS, and MOEN projects. Finally, we
474 use moored data obtained from [http://envofar.fo/data/index.php?dir=](http://envofar.fo/data/index.php?dir=Currents%2FADCP_Data&sort=N&order=A)
475 Currents%2FADCP_Data&sort=N&order=A and Moritz et al. (2021).

477 Appendix A. Mooring data

478 Appendix A.1. Faroe–Shetland Moorings

479 We obtained data from the bottom-mounted upward-looking ADCPs in-
480 stalled between Scotland and the Faroe Islands, used to monitor the Faroe-
481 Shetland Channel transport (Berx et al., 2013; Hansen et al., 2013, 2017).
482 These moorings are organised along three sections, which from west to east
483 are: NWZ (Cape Wrath to South Faroe), NWS (Fair Isle to Munken) and
484 NWE (Nolso to Muckle Flugga). The NWS line is one of the longest cur-
485 rent monitoring array timeseries in the Northeast Atlantic. For this study,

486 we use data from all three sections on the slope and shelf of the Scottish
487 side. At the NWSD site, we exclude measurements collected in 2014 during
488 the FASTNET campaign since the mooring position was displaced more than
489 fifteen kilometres away from its usual position. We further excluded deploy-
490 ments NWSD1011, NWSD0805, and NWSD0905 as we observed variance
491 issues. The data originating from the NWSE site suffered compass issues
492 between 2008 and 2013. These were corrected for by rotating the currents so
493 that M2 tidal ellipse directions were consistent throughout deployments (ma-
494 jor axis pointing $\sim 17^\circ$ anticlockwise from east). All Faroe-Shetland Channel
495 ADCP data were provided by Dr. Barbara Berx, at the exception of cur-
496 rents from NWSH, which were downloaded from [http://envofar.fo/data/
497 index.php?dir=Currents%2FADCP_Data&sort=N&order=A](http://envofar.fo/data/index.php?dir=Currents%2FADCP_Data&sort=N&order=A).

498 *Appendix A.2. OSNAP Moorings*

499 The Overturning in the Subpolar North Atlantic Program (OSNAP) is
500 an observational mooring array which monitors the strength of the Atlantic
501 Meridional Overturning Circulation between Scotland, Greenland, and New-
502 foundland. At the Rockall Trough eastern margin, two OSNAP moorings are
503 of relevance for the present study: RT-EB1 and RT-EB0. The former is a
504 mooring maintained since 2014 and equipped with six SPCMs sampling the
505 whole water column. Mooring RT-EB0 (sometimes referred to as ADCP1,
506 *e.g.* Houpert et al., 2020) was an 8-month upward-looking ADCP deployment
507 above the 750m isobath (approximately) in 2014–2015. Both moorings are lo-
508 cated at $\sim 57^\circ\text{N}$. Additionally, we use depth-averaged velocity from OSNAP
509 glider transects in the Rockall Trough eastern wedge (Fraser et al., 2022).
510 OSNAP moored and glider data were provided by Dr. Neil Fraser.

511 *Appendix A.3. LOIS-SES Moorings*

512 The Land Ocean Interaction Study – Shelf Edge Study (LOIS-SES) pro-
513 gram (Souza et al., 2001; Burrows and Thorpe, 1999) operated three long-
514 lasting moorings from Spring 1995 to Summer 1996 on the Hebridean slope,
515 as well as several shorter deployments which are not considered here. The
516 three rigs were located above the 140m, 400m, and 700m isobath at 56°27.6N
517 (Souza et al., 2001). The outer-shelf and shelf-edge moorings S140 and S400
518 were equipped with upward-looking ADCPs and functioned in a near con-
519 tinuous manner. The deeper mooring S700 was equipped with an array of
520 SPCMs and measured currents during Summer 1995, and from late Win-
521 ter to mid-Summer 1996, although only the period from Spring 1996 meets
522 the depth-averaging thresholds described in Section 2. The S400 ADCP
523 data, comprising of four deployments, notoriously suffers from compass bi-
524 ases (Huthnance et al., 2022). We manually re-aligned S400 data, so that
525 the semi-major axis of the residual flow variance is, for each deployment,
526 aligned with local isobaths (80°anticlockwise from east). The fourth and last
527 deployment (17 days in February 1996) was found too short-lived for such
528 editing and is not used here. The LOIS-SES historic data was retrieved from
529 BODC.

530 *Appendix A.4. OMEX Moorings*

531 The Ocean Margin EXchange (OMEX) program (Wollast and Chou,
532 2001) operated moorings on the Goban Spur and northwest of Ireland from
533 Spring 1993 to Autumn 1995 (White and Bowyer, 1997; Huthnance et al.,
534 2001; Pingree et al., 1999; van Aken et al., 2005). The currents were mea-
535 sured using SPCMs, allowing a partial depiction of the water column. Moor-

536 ing PML-154 meets our depth-averaging threshold and is included in our
537 analysis. We also use data from moorings PML-150, WBNE, and WBSW
538 because they fill in geographical gaps (regions of little measurements). PML-
539 150 had two SPCMs operated concurrently, but only for a four month period
540 during the Summer 1995. For this reason, we decided to retain only the
541 7-month long record of the top SPCM, located approximately 30 metres
542 from the sea surface. Northwest of Ireland (moorings WBNE and WBSW,
543 White and Bowyer, 1997), only the lowermost paddle wheel current-meters
544 (\sim 40m from the seabed) were recovered from the water, and we use them
545 here. The OMEX historic data was retrieved from the British Oceanographic
546 Data Centre (BODC).

547 *Appendix A.5. NOAC Mooring*

548 The NOrth Atlantic Changes (NOAC) observing array featured two in-
549 strumented moorings at its eastern boundary on the Goban Spur collecting
550 in-situ current data since 2016 (Moritz et al., 2021). GS-EB1 and GS-EB3
551 were located above the \sim 1530m and \sim 4450m isobaths respectively. We re-
552 trieval data from Moritz et al. (2021, Pangaea repository). GS-EB1 was
553 equipped with an upward-looking ADCP installed at mid-depth, and SPCMs
554 from 750 metres to the seabed. GS-EB3, equipped with SPCMs, does not
555 meet our depth-averaging thresholds and is not used here.

556 *Appendix A.6. ASPEX Moorings*

557 The Aquitaine/Armorican Shelves and Slopes Processes EXperiment (AS-
558 PEX) (Le Boyer et al., 2013; Kersalé et al., 2016) consisted in ten moorings
559 on the shelf and slope of the Bay of Biscay, operated between 2009 and

560 2011. Moorings were equipped with bottom-mounted upward-looking AD-
561 CPs and located on three sections orientated across the shelf and slope. The
562 northern sections (Penmarc'h and Loire) each featured three moorings above
563 the ~60m, ~130m and ~450m marks, while the 44°N section featured four
564 moorings above the ~50m, ~70m, ~130m and ~450m isobaths. ASPEX
565 ADCP data were contributed to the study by Dr. Louis Marié. The top
566 20% of ADCP bins were affected by surface reflection and removed following
567 Le Boyer et al. (2013).

568 *Appendix A.7. EirOOS Moorings*

569 We also include previously unpublished moored current data originat-
570 ing from the new EirOOS program and collected at three sites south and
571 west of Ireland by the Marine Institute and ‘A4’ ocean science group at
572 Maynooth University. The ‘South Rockall Trough Mooring’ (SRT) is located
573 in ~3000m of water off the western facade of the Porcupine Bank (15°31.2E,
574 52°59.9N) nearby a Met Éireann weather buoy named M6. A first deploy-
575 ment was conducted between October 2018 and June 2019 with two 75 kHz
576 RDI ‘Workhorse’ upward-looking ADCPs installed at ~400 and ~900 metres
577 below the water surface. During this pilot leg, the bottom ADCP malfunc-
578 tioned. Between May 2020 and June 2021, a second deployment with similar
579 configuration was carried out. A third leg was conducted between April 2022
580 and May 2023, with the line fitted with an upward-looking Nortek Signa-
581 ture 55 kHz ADCP installed at a depth of approximately a thousand metres.
582 Measurements at SRT are at present continued.

583 EBS5 (09°28.2E, 51°18.0N), a mooring located at proximity of the Fastnet
584 Rock off the southern Irish coast in approximately 90 metres of water, is in

585 continued operation since June 2020. It is equipped with a RDI 300 kHz
586 ‘Workhorse’ upward-looking ADCP installed within a trawl resistant bottom
587 mount. Here we used data from the first deployment leg, from June 2020 to
588 October 2021. During this time, the ADCP pressure sensor malfunctioned
589 and a nominal ADCP depth of 88m is used instead in the processing.

590 EBS1 was a mooring located in approximately 1000m of water depth on
591 the Goban Spur ($12^{\circ}11.1E$, $49^{\circ}06.8N$). It was equipped with a 75 kHz RDI
592 ‘Workhorse’ upward-looking ADCP installed approximately 600 metres be-
593 low the water surface. EBS1 was operated from March 2020 and discontinued
594 in October 2022, at the same time as the GS-EB1 and GS-EB3 of the NOAC
595 program (Moritz et al., 2021). It is noteworthy that EBS1 was located less
596 than a kilometre away from the position of the PML-154 mooring operated
597 from January 1994 to June 1995 as part of the OMEX program.

598 **Appendix B. Empirical Orthogonal Function analysis**

Let us define the geophysical anomaly (with respect to a climatological temporal mean) $\chi(x_1, x_2, \dots, x_m, t)$ a field of m spatial dimensions (say, two) and a temporal dimension.¹ The variables x_1, x_2, \dots, x_m and t are the coordinates which uniquely determine position in space and time. Such field χ can be objectively decomposed into modes of variability by means of Empirical Orthogonal Function Analysis, so that $\chi(x_1, x_2, \dots, x_m, t)$ can be formulated

¹A typical geophysical field variable has at least one and at most three spatial dimensions ($1 \leq m \leq 3$): for example, the sea surface height anomaly $\eta(x, y, t)$.

as

$$\chi(x_1, x_2, \dots, x_m, t) = \sum_i \phi_i(x_1, x_2, \dots, x_m) \alpha_i(t), \quad (\text{B.1})$$

599 where the Empirical Orthogonal Vectors or Functions (EOFs) ϕ carry the
 600 spatial information and the Principal Components (PCs) α the time varying
 601 development.

Typically, it is only possible to access discrete estimates of geophysical fields, meaning all χ dimensions have a finite length (n_1, n_2, \dots, n_m for space and n_t for time). Expressed in matrix notation, the decomposition takes the form

$$\boldsymbol{\chi} = \sum_{i=1}^n \phi_i \alpha_i, \quad (\text{B.2})$$

where, if $m > 1$, spatial dimensions of the variable χ are concatenated so that spatial dependence makes up a single dimension of length $n = n_1 + n_2 + \dots + n_m$. A decomposition of the form of Equation B.2 is sought such that 1) $\sum_{i=1}^k \phi_i \cdot \alpha_i$ tends towards χ in as little modes k as possible; and 2) the principal components have zero correlation between each other. These constraints are met when solving the eigenvalue – eigenvector problem

$$\mathbf{C} \phi_i = \lambda_i \phi_i \quad (\text{B.3})$$

with λ_i the i -eth eigenvalue and C the variance-covariance matrix of $\boldsymbol{\chi}$,

$$\mathbf{C} = \langle \boldsymbol{\chi} \boldsymbol{\chi}^T \rangle. \quad (\text{B.4})$$

The principal components α are obtained by projecting $\boldsymbol{\chi}$ on the eigenvector basis composed by the EOFs ϕ . This is done after the EOFs ϕ are scaled so that

$$\phi_i \cdot \phi_i = \lambda_i, \quad (\text{B.5})$$

which allows for the empirical orthogonal functions ϕ to have same physical dimension as χ and for the principal components α to have unit variance (Amabaum, 2004). In general, most of variability of χ is contained in a few leading modes $\phi_i \cdot \alpha_i$, so that EOF analysis can be used as a dimensionality reduction tool.

Appendix C. Current standard deviation ellipses

The EOF method described in Appendix B is an eigenvalue – eigenvector decomposition in the particular context of geophysics, which typically deal with fields of one to three spatial dimension(s) and a temporal dimension. In the general case, EOF decomposition is known as principal component analysis (PCA) and is not limited to spatio-temporal fields. Broadly speaking, PCA can be performed on any two-dimensional table $\chi = \chi(\mu, \kappa)$, where different $\mu \in [1, n]$ are different variables, and different κ are different realisations (or observations) of these variables. PCA allows for the objective reformulation of $\chi = \chi(\mu, \kappa)$ in a new coordinate basis made up of the orthogonal (hence uncorrelated) eigenvectors of the variance-covariance matrix \mathbf{C} . Note that again, this works at the conditions that all variables have zero-mean across the realisation dimension.

To compute the depth-averaged current standard deviation ellipses shown in Figure 1, χ is constructed so that

$$\chi^T = \begin{bmatrix} \bar{u}(t) \\ \bar{v}(t) \end{bmatrix} \quad (\text{C.1})$$

and a EOF/PC decomposition is performed, following the steps detailed in Appendix B (Equations B.2 to B.5). The scaled eigenvectors ϕ are obtained

and presented as the semi-major and semi-minor axes of the ellipses in Figure 1. Furthermore, in this simple scenario $n = 2$ (there are only two variables), meaning the principal component analysis is solely a rotation along the main direction of current variance and

$$\phi_1\alpha_1(t) + \phi_2\alpha_2(t) \quad (\text{C.2})$$

exactly equals $[\bar{u}(t), \bar{v}(t)]$.

Appendix D. Principal Component based Multiple Linear Regression (PCMLR)

Appendix D.1. System response to the wind forcing

In Section 3.2, we seek the sensitivity of the shelf sea-level variability (α_1) to the action of the wind stress, and for this purpose, we model the physical system as a (linear time-invariant) response to an external forcing,

$$\alpha_1(t) = \mathbf{K}\mathbf{X}, \quad (\text{D.1})$$

where the external forcing $\mathbf{X}(t)$ is a matrix composed of the zonal and meridional surface wind stress anomalies at each non-land grid point of the atmospheric reanalysis (τ^x, τ^y). \mathbf{K} represents the (time-invariant) response of the physical system, independent of wind large-scale co-variability and solely representing the ocean physics.

If the polluting noise in $\mathbf{X}(t)$ is assumed to be well-behaved, *i.e.* linearly independent of the signal in $\mathbf{X}(t)$, Equation D.1 is in fact a simple multiple linear regression,

$$\alpha_1(t) = \left(\sum_{i=1}^n k_i x_i(t) \right) + \mathcal{O}(t), \quad (\text{D.2})$$

with n the total number of predictors (that is, twice the number of non-land grid points, accounting for both zonal and meridional winds) and $\mathcal{O}(t)$ an independent noise. Equation D.1 can be solved in a least-square sense, allowing — in principle — to obtain a system response \mathbf{K} independent of the co-variability of the explanatory variables as desired,

$$\mathbf{K} = \langle \alpha_1 \mathbf{X}^T \rangle \langle \mathbf{X} \mathbf{X}^T \rangle^{-1}. \quad (\text{D.3})$$

where $\langle \mathbf{X} \mathbf{X}^T \rangle$ designates the covariance matrix of \mathbf{X} . In effect, because there is great co-variability in the wind stress signal at different grid points, the obtained \mathbf{K} is largely determined by the polluting noise, which is not in the general case well-behaved. Covariances between variables in \mathbf{X} are not perfectly known, and the obtained \mathbf{K} is strongly affected by the inaccuracy of the $\langle \mathbf{X} \mathbf{X}^T \rangle$ estimate. In this overfitting scenario, inferring causality from \mathbf{K} is impossible despite fitting α_1 is easily achieved. To circumnavigate this shortcoming, we opt for a change of variables based on principal component analysis (see also, Mendes, 2009).

Performing an eigen decomposition of the explanatory variable covariance matrix ($\langle \mathbf{X} \mathbf{X}^T \rangle = \Phi \Lambda \Phi^{-1}$, with $\Phi^{-1} = \Phi^T$) allows to write Equation D.3 as²

$$\mathbf{K} = \langle \alpha_1 \Gamma^T \rangle \Phi^T \Phi \Lambda^{-1} \Phi^T, \quad (\text{D.4})$$

where Γ is a matrix containing the wind stress anomalies principal components ($\mathbf{X} = \Phi \Gamma = \varphi_1(x, y)\gamma_1(t) + \dots + \varphi_n(x, y)\gamma_n(t)$). Equations D.3 and

²The eigenvalue decomposition here described is exactly similar to the EOF method for geophysical variables described in Appendix B.

D.4 are exactly equivalent, but the latter simplifies considerably to

$$\mathbf{Q} = \mathbf{K}\Phi = \langle\alpha_1\Gamma^T\rangle\Lambda^{-1}, \quad (\text{D.5})$$

which is a multiple linear regression onto the principal components of the wind stress anomalies:

$$\alpha_1(t) = \left(\sum_{i=1}^n q_i \gamma_i(t) \right) + \mathcal{O}(t). \quad (\text{D.6})$$

The sensitivity of α_1 to the wind variability is hence sought by solving the multiple linear regression of Equation D.6 to obtain \mathbf{Q} . Exclusion or inclusion in the regression of each of the principal components γ_i is objectively determined using the adjusted coefficient of determination R^2 ,

$$R^2 = 1 - \frac{\sum_{i=1}^{n_t} (\alpha_1 - \mathbf{Q}_T \Gamma_T)^2 (n_t - p)^{-1}}{\sum_{i=1}^{n_t} \alpha_1^2 (n_t - 1)^{-1}}, \quad (\text{D.7})$$

with Γ_T the matrix of explanatory principal components truncated of $m = n - p$ modes and n_t is the total number of temporal points. The system response \mathbf{K} is then obtained by projecting \mathbf{Q}_T onto the truncated eigenvector basis Φ_T (Eq. D.5). The method has the intrinsic interest that it does not leave ‘holes’ in the map of \mathbf{K} . Rather than having to remove grid points, higher eigen modes are removed.

We compute the sums in Equation D.7 over the total number of temporal points ($365 \text{ days} \times 29 \text{ years} = 10585 \text{ days}$), but estimate n_t in the bracket terms by dividing this value by the low-pass cut-off period (20 days); this gives a value of $n_t \approx 530$. A ‘leave-one-out’ procedure is then used to maximise R^2 (we do not test all possible combinations, but simply determine whether adding more principal components improve the R^2 or not), and we determine the best model includes the first $p = 81$ eigenvalues–eigenvectors.

651 *Appendix D.2. Significance test*

652 To test for the significance of the obtained patterns, we model \mathbf{K} at
 653 each and every grid point as a bivariate normal distribution with zero mean
 654 and unknown covariances ($\mathbf{K}_{ij} \sim \mathcal{N}(\boldsymbol{\mu}_0 = \mathbf{0}, \Sigma_{ij})$, where ij indicates the
 655 grid point). The rationale behind the choice to model $\mathbf{K}_{ij} = (K^x, K^y)$ as
 656 a normal distribution is that 1. the shelf mode principal component α_1 is
 657 approximately normally distributed (Figure 4 c); 2. \mathbf{K}_{ij} is obtained through
 658 linear combination of the α_1 elements (Equation D.4); and 3. a linear trans-
 659 formation of a normal distribution is also normal.

For readability, we will drop the notation $_{ij}$. The probability that $\mathbf{K} = (K^x, K^y)$ takes (X, Y) for values is

$$P(X, Y) = \frac{1}{2\pi\sqrt{|\Sigma|}} \exp\left(-\frac{\mathbf{X}^T \Sigma^{-1} \mathbf{X}}{2}\right), \quad (\text{D.8})$$

660 where $\Sigma = \mathbf{K}\mathbf{K}^T$ is the variance-covariance matrix of \mathbf{K} , $|\Sigma|$ the associated
 661 determinant and $\mathbf{X}^T = [X, Y]$. It is helpful to diagonalise Σ so that $\Sigma =$
 662 $\mathbf{B}\Lambda\mathbf{B}^T$, where \mathbf{B} is made up of the eigenvectors \mathbf{B}_1 and \mathbf{B}_2 and Λ is composed
 663 of the associated eigenvalues λ_1 and λ_2 .³

The probability Q that a random sample lies inside the ellipse of equi-
 probability $P = P(X, Y)$ is

$$Q = 1 - \exp\left(-\frac{(\mathbf{B}_1 \cdot \mathbf{X})^2}{2\lambda_1} - \frac{(\mathbf{B}_2 \cdot \mathbf{X})^2}{2\lambda_2}\right). \quad (\text{D.9})$$

³The eigenvalue–eigenvector decomposition here described is akin to the EOF method for vectors described in Appendix C.

664 Swapping \mathbf{X} for the true sensitivity \mathbf{K} in Equation D.9 allows to obtain
665 the significance of \mathbf{K} provided \mathbf{B} and $\mathbf{\Lambda}$ are estimated. For this purpose,
666 $M = 1000$ surrogates of the principal component α_1 were generated retain-
667 ing its Fourier transform magnitude but randomising its phase (similarly to
668 Ebisuzaki, 1997). These random timeseries were then used to generate M
669 sensitivity maps, following M -times the PCMLR method (note that for con-
670 sistency the number p of wind stress modes considered is kept unchanged at
671 81). The matrices \mathbf{B} and $\mathbf{\Lambda}$ are estimated at each map grid points from the
672 surrogate-obtained distribution, and significance is obtained.

673 **Appendix E. Seasonal modulation of the 20–360 day bandpass-
674 filtered sea-level variance**

675 The variance of the 20–360 day bandpass-filtered sea surface height is
676 generally greater in winter than in summer (not shown), in part because the
677 atmospheric forcing itself features seasonal changes in variance, but also for
678 other reasons (seasonal variations in stratification at the slope can also affect
679 the system response — in particular, they can change coastally trapped wave
680 characteristics, see Hughes et al., 2019; Mysak, 1980). EOF decomposition
681 assumes temporal stationarity in the covariance between sea surface height
682 observations at different gridpoints. Here, this signifies that the principal
683 components α carry *all* of the seasonal cycle in the sea-level variance, while
684 the empirical orthogonal functions ϕ do not carry any. Involved techniques
685 exist to circumvent this shortcoming (Kim and Wu, 1999; Kim et al., 2015,
686 2018), effectively rendering ϕ periodically time-dependent. In the present
687 case, this limitation is not a major issue as the seasonal cycle in the variance

is much smaller than the total variance. We simply note that α_1 tends to take extremum values (positives or negatives) more often in winter than in summer, and do not attempt to quantify how these changes affect the return-period statistics or the links with the atmospheric variability and in-situ currents.

References

- van Aken, H.M., Maas, L.R., van Haren, H., 2005. Observations of inertial wave events near the continental slope off Goban Spur. *Journal of physical oceanography* 35, 1329–1340.
- Ambaum, M.H.P., 2004. Calculating EOFs and principal component time-series.
- Ballarotta, M., Ubelmann, C., Pujol, M.I., Taburet, G., Fournier, F., Legeais, J.F., Faugère, Y., Delepoule, A., Chelton, D., Dibarboure, G., et al., 2019. On the resolutions of ocean altimetry maps. *Ocean Science* 15, 1091–1109.
- Berx, B., Hansen, B., Østerhus, S., Larsen, K.M., Sherwin, T., Jochumsen, K., 2013. Combining in situ measurements and altimetry to estimate volume, heat and salt transport variability through the Faroe–Shetland Channel. *Ocean Science* 9, 639–654.
- Burrows, M., Thorpe, S., 1999. Drifter observations of the hebrides slope current and nearby circulation patterns, in: *Annales Geophysicae*, Springer Verlag Göttingen, Germany. pp. 280–302.

- 709 Calafat, F.M., Chambers, D.P., Tsimplis, M.N., 2012. Mechanisms of decadal
710 sea level variability in the eastern North Atlantic and the Mediterranean
711 Sea. *Journal of Geophysical Research: Oceans* 117.
- 712 Chafik, L., Nilsen, J.E.Ø., Dangendorf, S., 2017. Impact of North Atlantic
713 teleconnection patterns on Northern European sea level. *Journal of Marine
714 Science and Engineering* 5, 43.
- 715 Chafik, L., Nilsen, J.E.Ø., Dangendorf, S., Reverdin, G., Frederikse, T., 2019.
716 North Atlantic Ocean circulation and decadal sea level change during the
717 altimetry era. *Scientific reports* 9, 1041.
- 718 Diabat , S.T., Fraser, N.J., White, M., McCarthy, G.D., in prep. On the
719 discontinuity of the European Slope Current.
- 720 Ebisuzaki, W., 1997. A method to estimate the statistical significance of a
721 correlation when the data are serially correlated. *Journal of Climate* 10,
722 2147–2153. doi:10.1175/1520-0442(1997)010<2147:AMTETS>2.0.CO;2.
- 723 Fraser, N.J., Cunningham, S.A., Drysdale, L.A., Inall, M.E., Johnson, C.,
724 Jones, S.C., Burmeister, K., Fox, A.D., Dumont, E., Porter, M., et al.,
725 2022. North Atlantic Current and European Slope current circulation
726 in the rockall trough observed using moorings and gliders. *Journal of
727 Geophysical Research: Oceans* , e2022JC019291.
- 728 Gill, A.E., Clarke, A.J., 1974. Wind-induced upwelling, coastal currents and
729 sea-level changes. *Deep-Sea Research and Oceanographic Abstracts* 21,
730 325–345. doi:10.1016/0011-7471(74)90038-2.

- 731 Gordon, R.L., Huthnance, J.M., 1987. Storm-driven continental shelf
732 waves over the Scottish continental shelf. Continental Shelf Research 7,
733 1015–1048. URL: <https://www.sciencedirect.com/science/article/pii/0278434387900975>, doi:[https://doi.org/10.1016/0278-4343\(87\)90097-5](https://doi.org/10.1016/0278-4343(87)90097-5).
- 735
- 736 Hansen, B., Larsen, K.M., Hátún, H., Kristiansen, R., Mortensen, E., Berx,
737 B., Sherwin, T., Østerhus, S., Quadfasel, D., Jochumsen, K., 2013. Mon-
738 itoring the flow of Atlantic water through the Faroe–Shetland Channel.
739 Technical Report. Havstovan Technical Report, 13–13, 22 p., available at:
740 <http://www.hav.fo>
- 741 Hansen, B., Poulsen, T., Húsgar Larsen, K.M., Hátún, H., Østerhus, S.,
742 Darelius, E., Berx, B., Quadfasel, D., Jochumsen, K., 2017. Atlantic water
743 flow through the Faroese Channels. Ocean Science 13, 873–888.
- 744 Hermans, T.H.J., Le Bars, D., Katsman, C.A., Camargo, C.M.L.,
745 Gerkema, T., Calafat, F.M., Tinker, J., Slangen, A.B.A., 2020. Drivers of interannual sea level variability on the Northwest-
746 ern European Shelf. Journal of Geophysical Research: Oceans
747 125, e2020JC016325. URL: <https://agupubs.onlinelibrary.wiley.com/doi/abs/10.1029/2020JC016325>, doi:<https://doi.org/10.1029/2020JC016325>. e2020JC016325 2020JC016325.
- 749
- 750
- 751 Hogarth, P., Hughes, C., Williams, S., Wilson, C., 2020. Improved and
752 extended tide gauge records for the British Isles leading to more consis-
753 tent estimates of sea level rise and acceleration since 1958. Progress in
754 Oceanography 184, 102333.

- 755 Holgate, S.J., Matthews, A., Woodworth, P.L., Rickards, L.J., Tamisiea,
756 M.E., Bradshaw, E., Foden, P.R., Gordon, K.M., Jevrejeva, S., Pugh,
757 J., 2013. New data systems and products at the permanent service for
758 mean sea level. *Journal of Coastal Research* 29, 493–504. doi:10.2112/
759 JCOASTRES-D-12-00175.1.
- 760 Houpert, L., Cunningham, S., Fraser, N., Johnson, C., Holliday, N.P., Jones,
761 S., Moat, B., Rayner, D., 2020. Observed variability of the North Atlantic
762 Current in the Rockall Trough from 4 years of mooring measurements.
763 *Journal of Geophysical Research: Oceans* 125, e2020JC016403.
- 764 Hughes, C.W., Fukumori, I., Griffies, S.M., Huthnance, J.M., Minobe, S.,
765 Spence, P., Thompson, K.R., Wise, A., 2019. Sea level and the role of
766 coastal trapped waves in mediating the influence of the open ocean on the
767 coast. *Surveys in Geophysics* 40, 1467–1492.
- 768 Huthnance, J.M., 1986a. The Rockall slope current and shelf-edge processes.
769 *Proceedings of the Royal Society of Edinburgh, Section B: Biological Sci-
770 ences* 88, 83–101.
- 771 Huthnance, J.M., 1986b. The subtidal behaviour of the Celtic Sea—III. a
772 model of shelf waves and surges on a wide shelf. *Continental Shelf Research*
773 5, 347–377. URL: <https://www.sciencedirect.com/science/article/pii/0278434386900038>, doi:[https://doi.org/10.1016/0278-4343\(86\)90003-8](https://doi.org/10.1016/0278-4343(86)90003-8).
- 776 Huthnance, J.M., Coelho, H., Griffiths, C.R., Knight, P.J., Rees, A.P., Sinha,
777 B., Vangriesheim, A., White, M., Chatwin, P.G., 2001. Physical structures,

- 778 advection and mixing in the region of goban spur. Deep Sea Research Part
779 II: Topical Studies in Oceanography 48, 2979–3021.
- 780 Huthnance, J.M., Hopkins, J., Berx, B., Dale, A., Holt, J., Hose-
781 good, P., Inall, M., Jones, S., Loveday, B.R., Miller, P.I., Polton,
782 J., Porter, M., Spingys, C., 2022. Ocean shelf exchange, NW Euro-
783 pean shelf seas: Measurements, estimates and comparisons. Progress
784 in Oceanography 202, 102760. URL: <https://www.sciencedirect.com/science/article/pii/S0079661122000222>, doi:<https://doi.org/10.1016/j.pocean.2022.102760>.
- 787 Kanamitsu, M., Ebisuzaki, W., Woollen, J., Yang, S.K., Hnilo,
788 J.J., Fiorino, M., Potter, G.L., 2002. NCEP–DOE AMIP-II
789 Reanalysis (R-2). Bulletin of the American Meteorological So-
790 ciety 83, 1631 – 1644. URL: <https://journals.ametsoc.org/view/journals/bams/83/11/bams-83-11-1631.xml>, doi:<https://doi.org/10.1175/BAMS-83-11-1631>.
- 793 Kersalé, M., Marie, L., Le Cann, B., Serpette, A., Lathuilière, C., Le Boyer,
794 A., Rubio, A., Lazure, P., 2016. Poleward along-shore current pulses on
795 the inner shelf of the Bay of Biscay. Estuarine, Coastal and Shelf Science
796 179, 155–171.
- 797 Kim, K.Y., Hamlington, B., Na, H., 2015. Theoretical foundation of cyclo-
798 stationary EOF analysis for geophysical and climatic variables: concepts
799 and examples. Earth-science reviews 150, 201–218.
- 800 Kim, K.Y., Lim, C.Y., Kim, E.J., 2018. A new approach to the space–time

- analysis of big data: application to subway traffic data in Seoul. *Journal of Big Data* 5, 5. URL: <https://doi.org/10.1186/s40537-018-0116-9>, doi:10.1186/s40537-018-0116-9.
- Kim, K.Y., Wu, Q., 1999. A comparison study of EOF techniques: Analysis of nonstationary data with periodic statistics. *Journal of Climate* 12, 185 – 199. URL: https://journals.ametsoc.org/view/journals/clim/12/1/1520-0442_1999_012_0185_acsoet_2.0.co_2.xml, doi:[https://doi.org/10.1175/1520-0442\(1999\)012<0185:ACSOET>2.0.CO;2](https://doi.org/10.1175/1520-0442(1999)012<0185:ACSOET>2.0.CO;2).
- Le Boyer, A., Charria, G., Le Cann, B., Lazure, P., Marié, L., 2013. Circulation on the shelf and the upper slope of the Bay of Biscay. *Continental Shelf Research* 55, 97–107.
- Mendes, M., 2009. Multiple linear regression models based on principal component scores to predict slaughter weight of broiler. *Archiv fur Geflugelkunde* 73, 139–144.
- Moat, B., Burmeister, K., Firing, Y., 2022. CLASS and OSNAP report for JC238. Technical Report. URL: https://nora.nerc.ac.uk/id/eprint/533744/1/JC238_cruise_report_final.pdf.
- Monahan, A.H., Fyfe, J.C., Ambaum, M.H., Stephenson, D.B., North, G.R., 2009. Empirical orthogonal functions: The medium is the message. *Journal of Climate* 22, 6501–6514.
- Moritz, M., Jochumsen, K., Kieke, D., Klein, B., Klein, H., Köllner, M., Rhein, M., 2021. Current meter measurement data and volume transport time series from deep-sea moorings deployed in the North Atlantic Eastern

- 824 Boundary (EB) region at Goban Spur. URL: <https://doi.org/10.1594/PANGAEA.932566>, doi:10.1594/PANGAEA.932566.
- 825
- 826 Moritz, M., Jochumsen, K., Kieke, D., Klein, B., Klein, H., Köllner, M.,
827 Rhein, M., 2021. Volume transport time series and variability of the North
828 Atlantic eastern boundary current at goban spur. *Journal of Geophysical
829 Research: Oceans* 126, e2021JC017393.
- 830 Mysak, L.A., 1980. Topographically trapped waves. *Annual Review of Fluid
831 Mechanics* 12, 45–76.
- 832 Permanent Service for Mean Sea Level, 2023. Tide gauge dataset. URL:
833 <http://www.psmsl.org/data/obtaining/>.
- 834 Pingree, R., Le Cann, B., 1989. Celtic and Armorican slope and shelf residual
835 currents. *Progress in Oceanography* 23, 303–338.
- 836 Pingree, R., Sinha, B., Griffiths, C., 1999. Seasonality of the European
837 slope current (Goban Spur) and ocean margin exchange. *Continental Shelf
838 Research* 19, 929–975.
- 839 Plag, H.P., Tsimplis, M., 1999. Temporal variability of the seasonal
840 sea-level cycle in the North Sea and Baltic Sea in relation to climate
841 variability. *Global and Planetary Change* 20, 173–203. URL: <https://www.sciencedirect.com/science/article/pii/S0921818198000691>,
842 doi:[https://doi.org/10.1016/S0921-8181\(98\)00069-1](https://doi.org/10.1016/S0921-8181(98)00069-1).
- 843
- 844 Pujol, M.I., Taburet, G., and SL-TAC team, 2023. QUID for sea level TAC
845 DUACS products. URL: <https://catalogue.marine.copernicus.eu/>

846 documents/QUID/CMEMS-SL-QUID-008-032-068.pdf. accessed: 2023-08-
847 01.

848 Souza, A.J., Simpson, J.H., Harikrishnan, M., Malarkey, J., 2001. Flow
849 structure and seasonality in the Hebridean slope current. Oceanologica
850 acta 24, 63–76.

851 White, M., Bowyer, P., 1997. The shelf-edge current north-west of Ireland,
852 in: Annales Geophysicae, Springer. pp. 1076–1083.

853 Wollast, R., Chou, L., 2001. Ocean margin exchange in the Northern Gulf
854 of Biscay: OMEX I. an introduction. Deep Sea Research Part II: Topical
855 Studies in Oceanography 48, 2971–2978.

856 Xu, W., Miller, P.I., Quartly, G.D., Pingree, R.D., 2015. Seasonality and
857 interannual variability of the European Slope Current from 20 years of
858 altimeter data compared with in situ measurements. Remote Sensing of
859 Environment 162, 196–207.

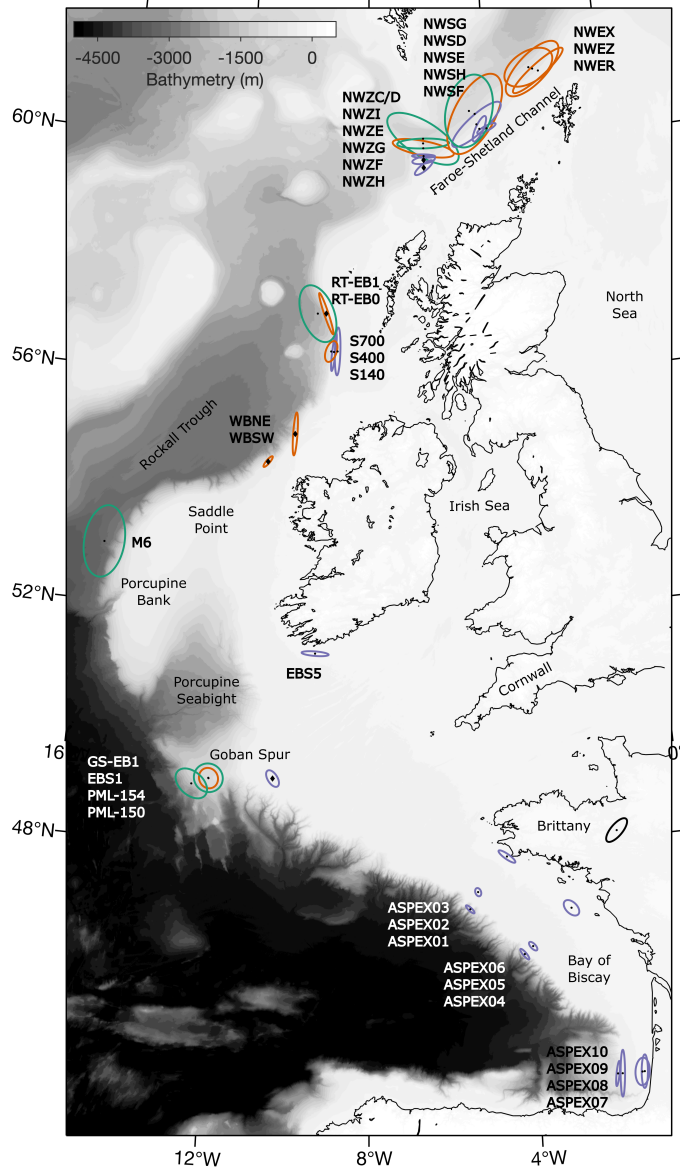


Figure 1: Bathymetry maps with markers indicating mooring positions and standard deviation ellipses of 20-day low-pass filtered in-situ current variability. The reference ellipse at $01^{\circ}41'E$, $48^{\circ}07'N$ has a semimajor axis radius of 5 cm.s^{-1} and a semiminor axis radius of 2 cm.s^{-1} . Moorings above the shelf and upper slope are indicated in purple, the ones over the intermediate slope in orange, and moorings in deeper waters are shown in green. At mooring sites indicated with diamond markers, standard deviation ellipses are shown for a single depth level (see text).

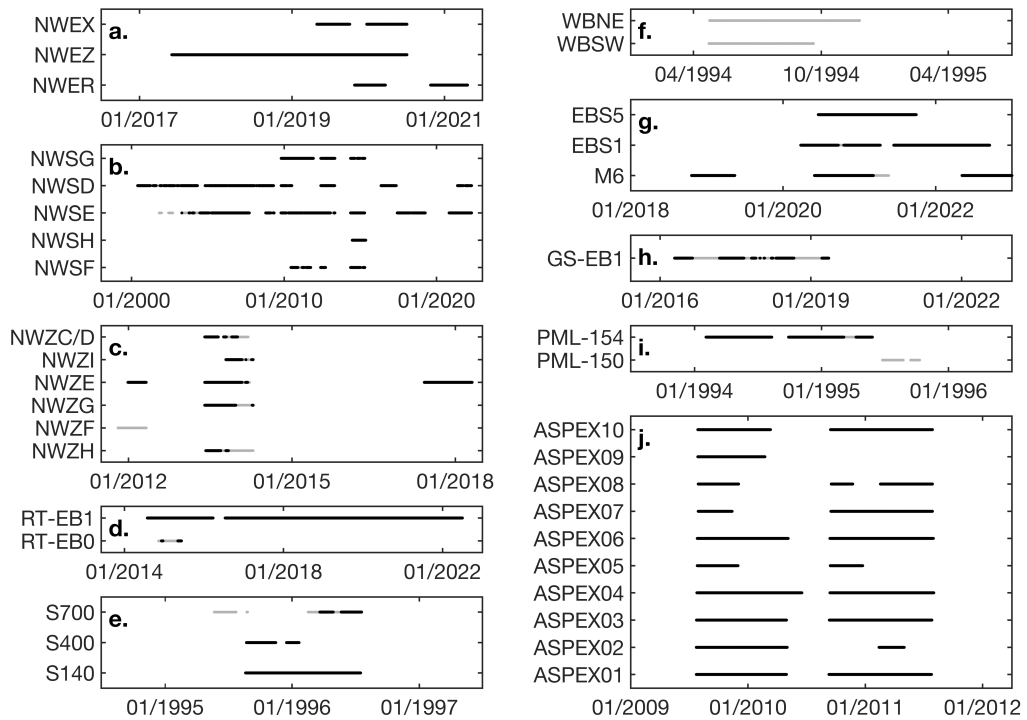


Figure 2: Temporal coverage of each of the mooring used in the present study. Black marker indicates, for each timestep, that a depth-averaged current could be computed, while grey line indicates that although a depth average could not be obtained, some information at this mooring is available. Note limits of the *x*-axes are different for each panel.

Program	Name	Location	Depth (m)	Source	Publication(s)
Faroe-Shetland Channel					
–	NWER	02°05.4W, 61°07.4N	490	Pers. Com.	–
–	NWEZ	02°17.5W, 61°09.3N	630	Pers. Com.	–
–	NWEX	02°25.0W, 61°11.0N	730	Pers. Com.	–
–	NWSF	04°00.1W, 60°12.0N	170	Pers. Com.	Berx et al. (2013); Hansen et al. (2013)
–	NWSH	04°14.4W, 60°11.9N	200	ENVOFAR	Berx et al. (2013); Hansen et al. (2013)
–	NWSE	04°20.3W, 60°16.6N	450	Pers. Com.	Berx et al. (2013); Hansen et al. (2013)
–	NWSD	04°22.5W, 60°27.2N	810	Pers. Com.	Berx et al. (2013); Hansen et al. (2013)
–	NWSG	04°33.9W, 60°29.7N	1050	Pers. Com.	Berx et al. (2013); Hansen et al. (2013)
–	NWZH	06°10.0W, 59°36.0N	210	Pers. Com.	–
–	NWZF	06°09.9W, 59°42.3N	210	Pers. Com.	Hansen et al. (2013)
–	NWZG	06°09.9W, 59°46.4N	370	Pers. Com.	Hansen et al. (2013)
–	NWZE	06°10.1W, 59°54.4N	780	Pers. Com.	Hansen et al. (2013)
–	NWZI	06°10.0W, 59°59.2N	1010	Pers. Com.	Hansen et al. (2013)
–	NWZC/D	06°10.1W, 60°04.0N	1100	Pers. Com.	Hansen et al. (2013)
Hebridean and Malin Seas					
OSNAP	RT-EB0	09°20.3W, 57°06.2N	750	Pers. Com.	Fraser et al. (2022); Houpert et al. (2020)
OSNAP	RT-EB1	09°36.0W, 57°06.0N	1800	Pers. Com.	Fraser et al. (2022); Houpert et al. (2020)
LOIS-SES	S140	08°58.0W, 56°28.0N	140	BODC	Souza et al. (2001); Xu et al. (2015); Huthnance et al. (2001)
LOIS-SES	S400	09°04.8W, 56°27.2N	400	BODC	Souza et al. (2001); Xu et al. (2015); Huthnance et al. (2001)
LOIS-SES	S700	09°09.8W, 56°27.7N	700	BODC	Souza et al. (2001)
OMEX	WBNE	10°12.0W, 55°02.5N	655	BODC	White and Bowyer (1997)
OMEX	WBSW	10°58.1W, 54°33.2N	668	BODC	White and Bowyer (1997)
West and southwest of Ireland					
EirOOS	SRT	15°31.2W, 52°59.9N	3010	–	–
OMEX	PML-150	10°30.9W, 49°09.0N	140	BODC	Pingree et al. (1999); Huthnance et al. (2001);
OMEX	PML-154	12°10.8W, 49°06.5N	1000	BODC	Pingree et al. (1999); Huthnance et al. (2001);
EirOOS	EBS5	09°28.2W, 51°18.0N	90	–	–
EirOOS	EBS1	12°11.1W, 49°06.8N	990	–	–
NOAC	GS-EB1	12°37.1W, 49°00.0N	1530	Moritz et al. (2021)	Moritz et al. (2021)
Bay of Biscay					
ASPEX	ASPEX01	04°30.2W, 47°47.7N	70	Pers. Com.	Le Boyer et al. (2013); Kersalé et al. (2016)
ASPEX	ASPEX02	05°16.0W, 47°12.6N	130	Pers. Com.	Le Boyer et al. (2013)
ASPEX	ASPEX03	05°28.9W, 46°55.4N	460	Pers. Com.	Le Boyer et al. (2013)
ASPEX	ASPEX04	02°57.3W, 46°51.6N	50	Pers. Com.	Le Boyer et al. (2013); Kersalé et al. (2016)
ASPEX	ASPEX05	03°58.1W, 46°15.0N	140	Pers. Com.	Le Boyer et al. (2013)
ASPEX	ASPEX06	04°11.0W, 46°7.3N	420	Pers. Com.	Le Boyer et al. (2013)
ASPEX	ASPEX07	01°30.8W, 44°00.1N	50	Pers. Com.	Le Boyer et al. (2013); Kersalé et al. (2016)
ASPEX	ASPEX08	01°34.0W, 43°59.9N	70	Pers. Com.	Le Boyer et al. (2013)
ASPEX	ASPEX09	02°01.9W, 44°00.0N	450	Pers. Com.	Le Boyer et al. (2013)
ASPEX	ASPEX10	02°08.6W, 44°00.1N	460	Pers. Com.	Le Boyer et al. (2013)

Table 1: Summary of mooring data used. Longitudes and latitudes are given in degrees-decimal minutes. Depths are averaged in case of several deployments, and approximated to the nearest ten. BODC is the British Oceanographic Data Centre. ENVOFAR is the Environmental Data on Terrestrial and Marine Ecosystems in the Faroe Islands. Pers.

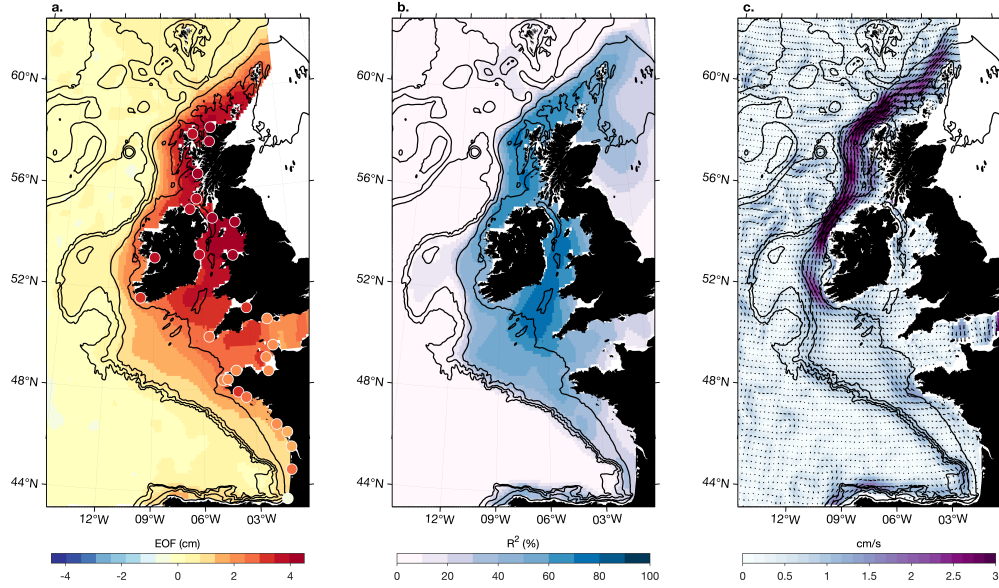


Figure 3: (a) The leading covariance-based EOF ϕ_1 of sea surface height anomaly over the domain (colour shadings). (b) The variance explained (in percent) by the leading principal component α_1 at each grid point, obtained by squaring the correlation between α_1 and local sea surface height changes. (c) The surface geostrophic currents associated with the mode, $\mathbf{v} = -g\mathbf{k} \times \nabla(\phi_1)/f$. On (a), coloured circular markers present the regression coefficients of the tide gauge timeseries versus the principal component α_1 . On all three maps, black contour lines indicate bathymetry levels 200m (the shelf-edge), 1000m and 2000m.

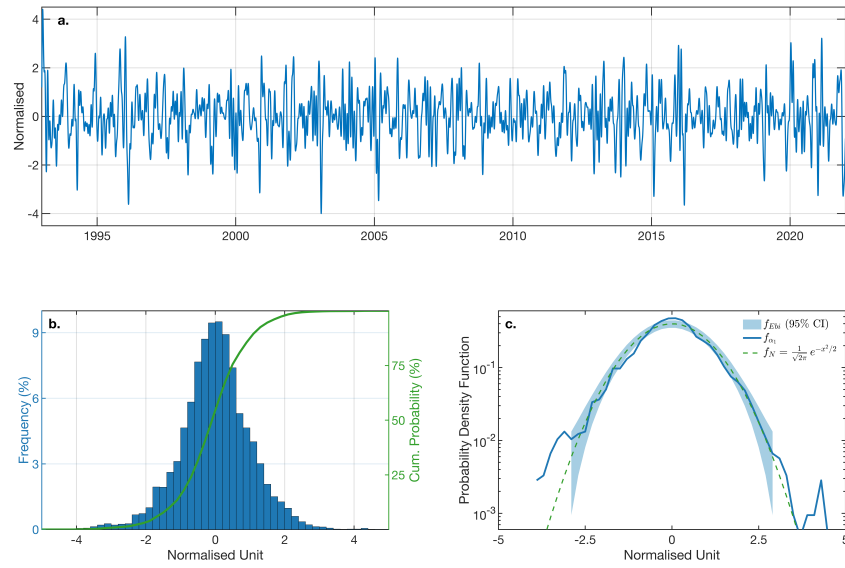


Figure 4: (a) The leading principal component α_1 or timeseries of the mode. (b) The histogram of α_1 (blue bars), and the associated probability of α_1 being below a given threshold (green line). (c) Estimated probability density function f_{α_1} in logarithmic scale (dark blue line), together with 95% confidence interval of randomly obtained probability density function f_{Ebi} (light blue area), and the standard normal distribution probability density function (dashed green line). Note the timeseries randomly created using the Ebisuzaki (1997) method and used to test significance have a distribution which is approximately normal (Panel c.).

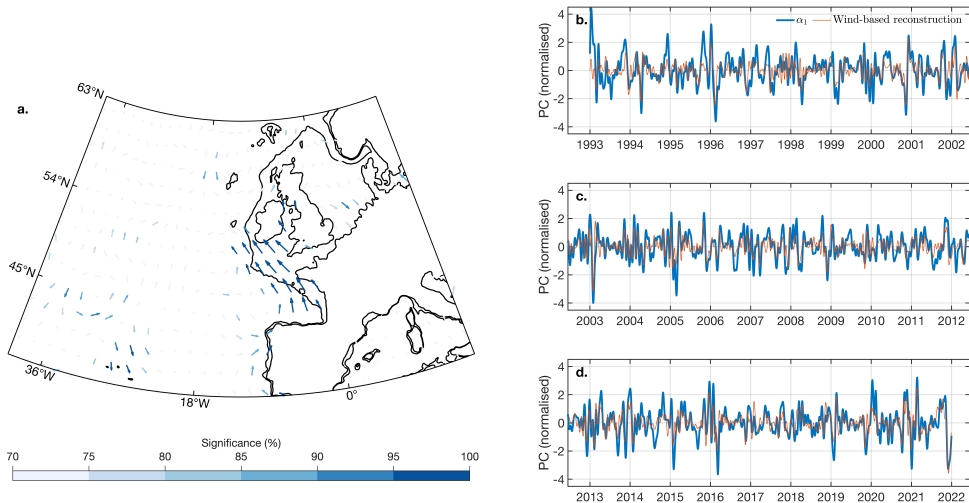


Figure 5: (a) The sensitivity $\mathbf{K}(x, y)$ of shelf sea-level changes — more exactly, α_1 — to wind stress variations in the Northeast Atlantic. Significance, which is obtained using a modified Ebisuzaki (1997) approach (see text), is indicated as shades of colours. This map should be read recalling the dot product in Equation 3. When wind stress anomaly vectors exactly ‘line-up’ with \mathbf{K} , the shelf sea level is high. At the other extreme, during period when wind stress anomaly vectors oppose \mathbf{K} , largely negative sea levels are obtained over the shelf. When the wind field is in no particular arrangement with respect to \mathbf{K} , the principal component α_1 takes values closer to zero. (b, c and d) The sea-level mode principal component α_1 is shown as a blue line together with the wind-based fit, which is obtained by summing wind stress anomalies projected along the sensitivity \mathbf{K} , retaining only significant ($> 95\%$) grid points in the box 18°W , 44°N to 0°W , 60°N (orange line).

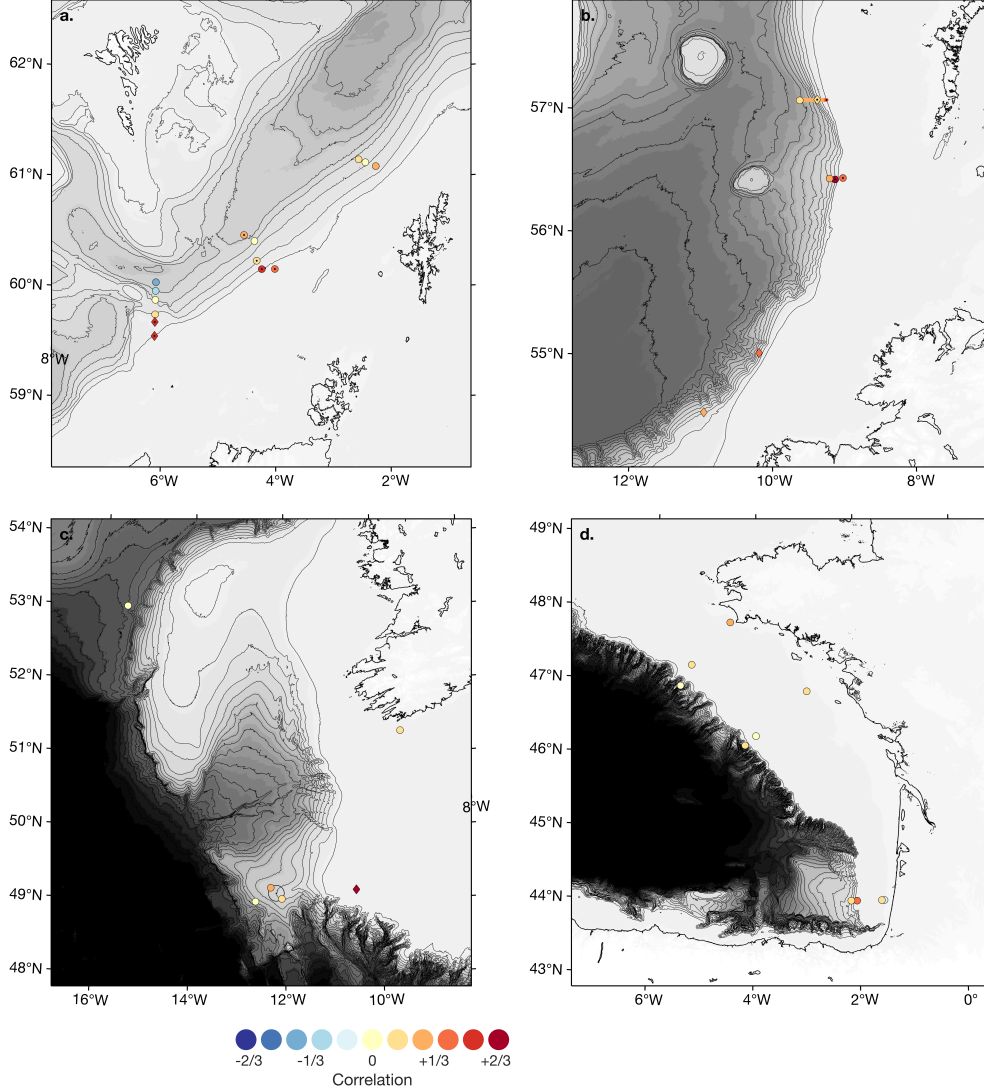


Figure 6: Correlation between depth-averaged in-situ velocities projected along-isobath and the common mode principal component α_1 in the four regions (circular markers). Diamond markers indicate correlations obtained with velocities measured at a single level rather than with depth-averaged currents (see text). Significance above the 95% level is indicated by black dots. In (c), PML-154 and EBS1 on the Goban Spur are, for readability, shown displaced from their original position (the central dot). Correlations with velocities obtained from Fraser et al. (2022) glider section are also shown on (b), underneath the mooring markers. On all panels, isobaths are indicated every 200m by thin black contours.

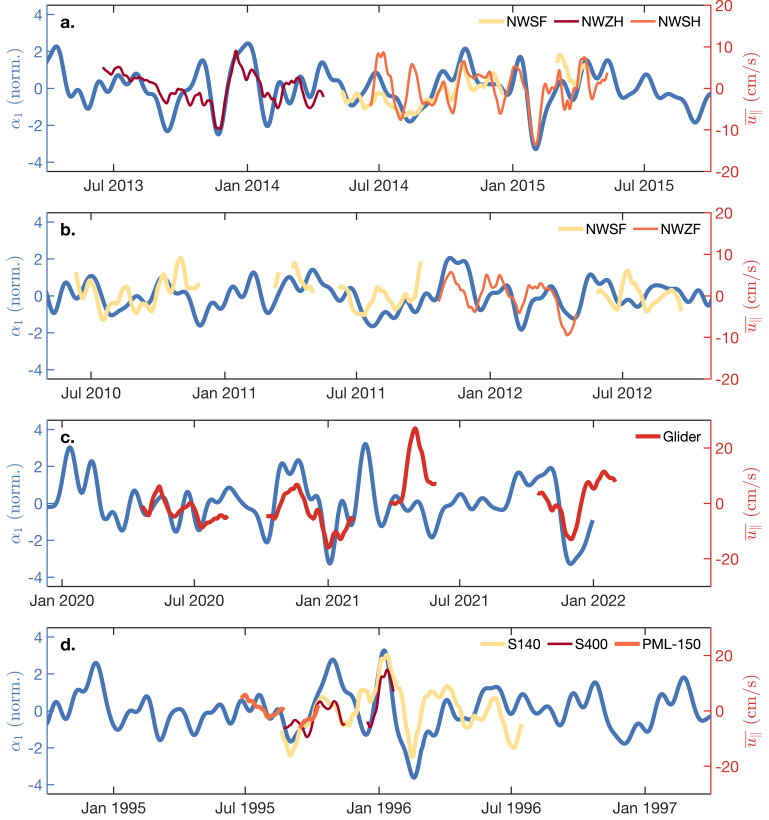


Figure 7: Principal component α_1 against in-situ along-isobath current anomalies. Currents are depth-averaged everywhere, except for moorings PML-150, NWZH, and NWZF (see text). On b., glider-obtained depth-averaged velocities are averaged over the 365–195 metre isobath range.